

Fluid-structure interactions (FSI) are very common in many natural processes and engineering applications. However, modeling FSI with large structural deformations and turbulence flows under high Reynolds number (Re) is still a challenging task. Here, we present a hybrid 3D model that combines the advantages of Lattice Boltzmann Method (LBM) on solving complex flow problems and the capability of Material Point Method (MPM) on handling large structural deformations. A sharp interface coupling scheme is presented in details and a LES sub-grid model is adapted for turbulent flows. The structure solver is validated by comparing with Euler beam theory and the fluid solver is tested for fluid round circle and cube obstacles under a large range of Re . The coupled model is validated by simulations of a flexible plate deformation in shear flows. Good agreements are found comparing with experimental results. Finally some applications of importing realistic geometries from Computer Assisted Design (CAD) software, are shown to demonstrate the future applications of the method.

Coupled Material Point Lattice Boltzmann Method for modeling fluid-structure interactions with large deformations.

Pei Zhang^a, Siqi Sun^a, Yilin Chen^b, Weicheng Cui^{a,**}, S.A. Galindo-Torres^{a,*}

^a*Key Laboratory of Coastal Environment and Resources Research of Zhejiang Province,
School of Engineering, Westlake University, Hangzhou, China*

^b*State Key Laboratory of Hydrology-Water Resources and Hydraulic Engineering, Hohai
University, Nanjing, China*

1. Introduction

Fluid-structure interaction (FSI) problems can be widely found in both natural processes and engineering applications. Examples include wings of birds and insects interact with surrounding airs [1], motions of floating wind turbines in deep sea [2] and fish swimming [3]. Furthermore, many biological systems involve FSI processes like the transport and deformation of red blood cells [4] and cell migration in tumors [5]. Besides their importance, understanding these FSI processes is still a challenging task due to their complex dynamics. Particularly, when the structural deformations are considerable large under high Reynolds number, where the flows and structure motions are strongly coupled.

Many numerical models are developed to simulate FSI problems with some success [6–12]. These models can be classified into two categories depending on the mesh strategies. The first approach use body fitting meshes where the mesh always coincides with the deformable structure boundaries [13, 14]. It is also referred to as the monolithic approach since fluid and structure motions are solved within the same equation systems. This approach can achieve high accuracy and numerical stability due to the exact description of structure boundaries [6, 13, 14]. However, it also suffers from high compu-

*s.Torres@westlake.edu.cn

**cuiweicheng@westlake.edu.cn

tational cast since mesh regenerations are frequently required, particularly when large deformations occur. On the other hand, fixed meshes are adapted in the second approach where the governing equations of fluid and structures are solved separately. Since the structure boundaries are generally not on the fixed mesh nodes, the influence of structure motions on the fluid is introduced to nodes that near to solid boundaries. For example, the widely used Immersed Boundary Method (IBM) [15] replaces the structure effects by an external force field. IBM schemes can be classified into diffuse interface IBMs [9, 16] and sharp interface IBMs [17, 18]. However, penetrating streamlines are often found for diffuse interface IBMs particularly for explicit schemes [9]. The second approach is adapted here since it is most suited for practical problems [19].

In this work, the flows are modelled by the Lattice Boltzmann Method (LBM). LBM has emerged as an effective approach of Computational Fluid Dynamics (CFD) during the last decades, and it has attracted numerous interests in simulating complex flows including FSI [6, 20]. The success of LBM is mainly contributed by several unique advantages. First, the solution of advection in LBM is exact which reduce the numerical diffusion errors in conventional CFD methods [21]. Second, the locality of the collision operator guarantees a high parallelization efficiency of LBM codes. LBM is also capable to efficiently handle complex moving boundary conditions. For example, Zhang et al. [22] studied the settling of particles with complex shapes with LBM. Furthermore, LBM can be easily coupled with other numerical schemes like the Discrete Element Method (DEM) [23–26] for fluid-particle interactions and the Finite Element Method (FEM) [6, 27, 28] for deformable structures. Recently, Liu et al. [12] coupled LBM with the Material Point Method (MPM) for 2D FSI problems with large structural deformations.

For structure dynamics, the Material Point Method (MPM) which can handle structure large deformations is adapted. MPM origins from the particle-in-cell Method [29] and is first introduced by Sulsky [30] for solid mechanics. As a hybrid method, MPM shares features of both meshfree methods (Smoothed Particle Hydrodynamics [31], Element Free Galerkin Method [32]) and grid-based methods (FEM). The space discretization is similar to meshfree methods where the solid structure is represented by a set of material points. Historical information like mass, density, momentum, strains and stresses are carried by material points. However, unlike classical meshfree methods, material points do not directly interact with each other in MPM. Instead, a background mesh is employed to solve governing

equations in a FEM fashion. The information transformation between material points and the background mesh is achieved by interpolations with the help of shape functions. The advantages of MPM can be summarized in the following aspects: MPM can handle large deformation problems due to its particle representation and the mesh distortion problems in classical FEM are avoided [33]. MPM is an efficient scheme since it does not require the expansive neighbour searching procedure which is essential for pure meshfree methods. Furthermore, applying boundary conditions in MPM is easy and identical to FEM, which is not so straightforward in meshfree methods.

LBM have been successfully coupled with structure solvers in previous studies. For instance, Rosis et al. [6] proposed three coupling schemes for LBM and FEM, both explicit and implicit schemes are considered. It is found that all these coupling scheme can achieve decent accuracy and numerical stability. The best accuracy is achieved by the implicit coupling scheme with the highest computational cost. The enhanced explicit coupling scheme is a good choice if the computational cost is the bottleneck.

The goal of this work is to provide a coupled model that combines the efficiency of LBM on solving flows and the capability of MPM on handling large deformations for simulating FSI problems with large deformation under a broad range of Reynolds numbers.

2. Problem statement

The study aims to model interactions between single phase fluid and fully immersed structure. The weakly compressible Newtonian fluid is considered and flows can be described by the Boltzmann's kinetic equation.

For structure dynamics, the material is assumed to be isotropic, homogeneous and follows linear elastic law. The structure motions are governed by mass and linear momentum conservation equations.

At the fluid-structure interface, equilibrium and geometrical compatibility are assumed [6]. The non-slipping condition should be satisfied: the fluid velocity equals to the structure velocity at the interface. Due to the Newton's third law, the total traction on the fluid boundary has same magnitude but with opposite direction as the total traction on the structure boundary.

3. Numerical model

3.1. Material Point Method

The structure motions are governed by Eq. 1, where ρ_s , \mathbf{u}_s , $\boldsymbol{\sigma}_s$, \mathbf{b}_s and \mathbf{f}_s^h are the density, velocity, Cauchy stress tensor, body force and hydrodynamic force of the structure. The subscript s stands for properties of the structure, it is omitted in rest of this section for readability. Eq. 1 is discretized and solved by MPM. These are four major procedures of MPM: 1) Mapping information from particles to the mesh. 2) Solving governing equations on the mesh. 3) Mapping information from the mesh back to particles. 4) Updating stress on particles. In the following the subscripts p and I stand for properties of particles and nodes respectively.

$$\begin{cases} \frac{D\rho_s}{Dt} + \rho_s \nabla \cdot \mathbf{u}_s = 0, \\ \rho_s \frac{D\mathbf{u}_s}{Dt} = \nabla \cdot \boldsymbol{\sigma}_s + \rho_s \mathbf{b}_s + \mathbf{f}_s^h, \end{cases} \quad (1)$$

1) Mapping information from particles to the mesh nodes. The nodal mass m_I , momentum $m_I \mathbf{u}_I$, external force \mathbf{f}_I^{ext} and internal forces \mathbf{f}_I^{int} are interpolated as following:

$$\begin{aligned} m_I &= \sum_p \phi_I(\mathbf{x}_p) m_p, \\ m_I \mathbf{u}_I &= \sum_p \phi_I(\mathbf{x}_p) m_p \mathbf{u}_p, \\ \mathbf{f}_I^{ext} &= \mathbf{f}_h(\mathbf{x}_I) + \sum_p \phi_I(\mathbf{x}_p) m_p \mathbf{b}, \\ \mathbf{f}_I^{int} &= - \sum_p V_p \boldsymbol{\sigma} \nabla \phi_I(\mathbf{x}_p) \end{aligned} \quad (2)$$

Where $\phi_I(\mathbf{x}_p)$ is the effective grid shape function that evaluated at \mathbf{x}_p . m_p , \mathbf{u}_p and V_p are the particle mass, velocity and volume. \mathbf{f}_I^{ext} and \mathbf{f}_I^{int} are the external and internal force. \mathbf{b} is the body force (like gravity) and the nodal hydrodynamic force \mathbf{f}_h is used to couple with fluid solver later.

2) Solving the momentum equations at the background mesh:

$$\begin{aligned} (m_I \mathbf{u}_I)^{t+\Delta t_{MPM}} &= (m_I \mathbf{u}_I)^t + \mathbf{f}_I^t \Delta t_{MPM}, \\ \mathbf{u}_I^{t+\Delta t_{MPM}} &= \frac{(m_I \mathbf{u}_I)^{t+\Delta t_{MPM}}}{m_I^t}, \end{aligned} \quad (3)$$

Where the total force is given by $\mathbf{f}_I = \mathbf{f}_I^{ext} + \mathbf{f}_I^{int}$. The Dirichlet boundary conditions are applied in this step as: $(m_I \mathbf{u}_I)^{t+\Delta t_{MPM}} = \mathbf{0}$ and $\mathbf{f}_I^t = \mathbf{0}$.

3) Mapping information from nodes back to particles and update particle position, velocity:

$$\begin{aligned}\mathbf{x}_p^{t+\Delta t_{MPM}} &= \mathbf{x}_p^t + \Delta t_{MPM} \sum_I \phi_I(\mathbf{x}_p^t) \frac{(m_I \mathbf{u}_I)^{t+\Delta t_{MPM}}}{m_I^t}, \\ \mathbf{u}_p^{t+\Delta t_{MPM}} &= \mathbf{u}_p^t + \Delta t_{MPM} \sum_I \phi_I(\mathbf{x}_p^t) \frac{\mathbf{f}_I^{t+\Delta t_{MPM}}}{m_I^t},\end{aligned}\tag{4}$$

4) Update particle stresses:

$$\begin{aligned}\mathbf{L}_p^{t+\Delta t_{MPM}} &= \sum_I \phi_I(\mathbf{x}_p^t) \mathbf{u}_I^{t+\Delta t}, \\ \mathbf{F}_p^{t+\Delta t_{MPM}} &= \left(\mathbf{I} + \mathbf{L}_p^{t+\Delta t_{MPM}} \Delta t_{MPM} \right) \mathbf{F}_p^t, \\ V_p^{t+\Delta t_{MPM}} &= \det(\mathbf{F}_p^{t+\Delta t_{MPM}}) V_p^0, \\ \boldsymbol{\sigma}_p^{t+\Delta t_{MPM}} &= \boldsymbol{\sigma}_p^t + \left(\Delta \boldsymbol{\sigma}_p + \boldsymbol{\sigma}_p^t \cdot \mathbf{W}^T + \mathbf{W} \cdot \boldsymbol{\sigma}_p^t \right) \Delta t_{MPM}\end{aligned}\tag{5}$$

Where \mathbf{L}_p and \mathbf{F}_p are the velocity gradient and deformation gradient tensors. The strain rate tensor $\Delta \boldsymbol{\epsilon}$ and rotation rate tensor \mathbf{W} are given by $\Delta \boldsymbol{\epsilon} = \frac{1}{2}(\mathbf{L} + \mathbf{L}^T)$, $\mathbf{W} = \frac{1}{2}(\mathbf{L} - \mathbf{L}^T)$, which are the inputs for the constitutive model to calculate stress rate $\Delta \boldsymbol{\sigma}$. The linear elastic model for homogeneous and isotropic materials is adapted here: $\Delta \boldsymbol{\sigma}_p = \mathbf{C}_e : \Delta \boldsymbol{\epsilon}$. The elasticity tensor \mathbf{C}_e is given as:

$$\mathbf{C}_e = \frac{E}{(1-\nu_s)(1-2\nu_s)} \begin{bmatrix} 1-\nu_s & \nu_s & \nu_s & 0 & 0 & 0 \\ \nu_s & 1-\nu_s & \nu_s & 0 & 0 & 0 \\ \nu_s & \nu_s & 1-\nu_s & 0 & 0 & 0 \\ 0 & 0 & 0 & \frac{1-2\nu_s}{2} & 0 & 0 \\ 0 & 0 & 0 & 0 & \frac{1-2\nu_s}{2} & 0 \\ 0 & 0 & 0 & 0 & 0 & \frac{1-2\nu_s}{2} \end{bmatrix}\tag{6}$$

Where E is the Young's modulus and ν_s is the Poisson ratio.

3.1.1. CPDI scheme

The original MPM uses the linear hat shape function [29] which suffers from the crossing error. It often occurs when the material points move across

the cell boundaries [34]. The main reason of crossing errors is the discontinuity of the shape function gradient. One popular solution to address this issue is adapting the generalized interpolation material point method (GIMP) [34] where a smoother shape function is used. The GIMP shape function and its gradient are defined as:

$$\begin{aligned}\phi_I(\mathbf{x}_p) &= \frac{1}{V_p} \int_{\Omega_p} \chi(\mathbf{x} - \mathbf{x}_p) S_I(\mathbf{x}) d\mathbf{x}, \\ \nabla \phi_I(\mathbf{x}_p) &= \frac{1}{V_p} \int_{\Omega_p} \chi(\mathbf{x} - \mathbf{x}_p) \nabla S_I(\mathbf{x}) d\mathbf{x}\end{aligned}\tag{7}$$

Where $S_I(\mathbf{x})$ is the linear hat shape function, $\chi(\mathbf{x})$ and Ω_p are the particle characteristic function and its support domain. It can be seen that Eq. 7 recovers to standard MPM shape function if the Dirac delta function is chosen as the particle characteristic function. Classical GIMP employs the piece-wise constant particle characteristic function:

$$\chi(\mathbf{x}) = \begin{cases} 1 & \mathbf{x} \in \Omega_p \\ 0 & \text{otherwise} \end{cases}\tag{8}$$

Many variants of GIMP are developed to solve Eq. 7. The main difference lays on how to update the particle domain Ω_p . Ω_p can be treated as time-independent in the unchanged GIMP (uGIMP). It is updated by using the deformation gradient \mathbf{F} with (contiguous particle GIMP) or without considering the shear deformation. Overall, these GIMP schemes relief the crossing errors but also have their shortcomings. For instance, extension instabilities are reported for uGIMP under large particle separations. Also, gaps and overlapping between support domains are inevitable under general loading conditions [35].

The latest development of GIMP scheme is CPDI (Convected Particle Domain Interpolation) [35]. By introducing additional corners, the particle domains can be tracked without gaps and overlapping with others. Nguyen et al. [33] further extend CPDI with varies types of particle domains for both 2D (triangle, quadrilateral, and polygon) and 3D (tetrahedron and polyhedron). Here, the linear tetrahedron elements are used to represent the particle domains since it is convenient to describe complex 3D geometries. The alternative shape function for tetrahedron elements is constructed by interpolating standard shapes functions at corners:

$$S_I^{app}(\mathbf{x}) = \sum_{c=1}^4 M_c(\mathbf{x}) S_I(\mathbf{x}_c) \quad (9)$$

\mathbf{x}_c is the corner position and $M_c(\mathbf{x})$ are the shape functions of corners. The CPDI shape function and its gradient can be obtained by substituting Eq. 9 to Eq. 7:

$$\begin{aligned} \phi_I(\mathbf{x}_p) &= \frac{1}{V_p} \sum_{c=1}^4 \left[\int_{\Omega_p} M_c(\mathbf{x}) d\mathbf{x} \right] S_I(\mathbf{x}_c) = \sum_{c=1}^4 w_c^f S_I(\mathbf{x}_c), \\ \nabla \phi_I(\mathbf{x}_p) &= \frac{1}{V_p} \sum_{c=1}^4 \left[\int_{\Omega_p} \nabla M_c(\mathbf{x}) d\mathbf{x} \right] S_I(\mathbf{x}_c) = \sum_{c=1}^4 \mathbf{w}_c^g S_I(\mathbf{x}_c) \end{aligned} \quad (10)$$

Where w_c^f and \mathbf{w}_c^g are the weighting and gradient weighting functions which are given accordingly:

$$\begin{aligned} w_i^f &= \frac{1}{4}, \\ \mathbf{w}_i^g &= \frac{1}{6V_p} [a_i, b_i, c_i]^T \end{aligned} \quad (11)$$

And

$$\begin{aligned} a_1 &= y_{42}z_{32} - y_{32}z_{42}, a_2 = y_{31}z_{43} - y_{34}z_{13}, \\ a_3 &= y_{24}z_{14} - y_{14}z_{24}, a_4 = y_{13}z_{21} - y_{12}z_{31}, \\ b_1 &= x_{32}z_{42} - x_{42}z_{32}, b_2 = x_{43}z_{31} - x_{13}z_{34}, \\ b_3 &= x_{14}z_{24} - x_{24}z_{14}, b_4 = x_{21}z_{13} - x_{31}z_{12}, \\ c_1 &= x_{42}y_{32} - x_{32}y_{42}, c_2 = x_{31}y_{43} - x_{34}y_{13}, \\ c_3 &= x_{24}y_{14} - x_{14}y_{24}, c_4 = x_{21}y_{13} - x_{31}y_{12}, \\ 6V_p &= x_{21}(y_{23}z_{34} - y_{34}z_{23}) + x_{32}(y_{34}z_{12} - y_{12}z_{34}) + x_{43}(y_{12}z_{23} - y_{23}z_{12}) \end{aligned} \quad (12)$$

Where $x_{ij} = x_i - x_j$, $y_{ij} = y_i - y_j$ and $z_{ij} = z_i - z_j$. x_i , y_i and z_i are the coordination of i th corner of the tetrahedron. The order of corners are arranged to make sure that the signed volume V_p stays positive [33].

3.2. Lattice Boltzmann Method

The fluid flow is simulated by the Lattice Boltzmann equation (LBE) – a discretized form of the Boltzmann equation [24, 36, 37]. The D3Q15 model

is used with the space divided into cubic lattices. The velocity domain is discretized to fifteen velocity vectors as shown in Figure 1. The discrete velocity vectors are defined as follows:

$$\mathbf{e}_i = \begin{cases} 0, & i = 0, \\ (\pm C, 0, 0), (0, \pm C, 0), (0, 0, \pm C), & i = 1 \text{ to } 6, \\ (\pm C, \pm C, \pm C), & i = 7 \text{ to } 14, \end{cases}$$

where $C = \Delta x_{LBM} / \Delta t_{LBM}$ being the characteristic lattice velocity (Δx_{LBM} is the lattice size).

Based on the Chapman-Enskog expansion of the Boltzmann equation, an evolution rule is applied to every distribution function [38]:

$$f_i(\mathbf{x} + \mathbf{e}_i \Delta t_{LBM}, t + \Delta t_{LBM}) = f_i(\mathbf{x}, t) + \Omega_{col}, \quad (13)$$

where f_i is the probability distribution function, \mathbf{x} is the position of the local lattice, Δt is the time step and Ω_{col} is the collision operator. The well-known Bhatnagar-Gross-Krook (BGK) collision operator is used in this study,

$$\Omega_{col} = \frac{\Delta t_{LBM}}{\tau} (f_i^{eq} - f_i), \quad (14)$$

where τ is the relaxation time and f_i^{eq} is the equilibrium distribution given by,

$$f_i^{eq} = \omega_i \rho_f \left(1 + 3 \frac{\mathbf{e}_i \cdot \mathbf{u}_f}{C^2} + \frac{9(\mathbf{e}_i \cdot \mathbf{u}_f)^2}{2C^4} - \frac{3u_f^2}{2C^2} \right), \quad (15)$$

The weights are $\omega_0 = 2/9$, $\omega_i = 1/9$ for $i = 1$ to 6, $\omega_i = 1/72$ for $i = 7$ to 14. The kinetic viscosity is related to the relaxation time by

$$\nu = \frac{(\Delta x_{LBM})^2}{3\Delta t_{LBM}} \left(\tau - \frac{1}{2} \right), \quad (16)$$

Here the Mach number is defined as the ratio of the maximum velocity to C . When $Ma \ll 1$, the LBE can be recovered to the Navier-Stokes equation. More detail can be found in [39]. The macroscopic properties of fluid such as density ρ and flow velocity \mathbf{u} can be determined by the zero-th and the first order moment of the distribution function:

$$\begin{aligned} \rho_f(\mathbf{x}) &= \sum_{i=0}^{14} f_i(\mathbf{x}), \\ \mathbf{u}_f(\mathbf{x}) &= \frac{1}{\rho_f(\mathbf{x})} \sum_{i=0}^{14} f_i(\mathbf{x}) \mathbf{e}_i, \end{aligned} \quad (17)$$

It is well known that the stability of the LBM simulation is affected by the relaxation time τ . The value of τ should not be too close to 0.5 because of the use of a linearized BGK collision operator [24]. Due to this limitation, the standard Lattice Boltzmann method is only suitable for flow at relatively low Reynolds numbers. This problem can be relieved by adapting sophisticated collision models like Multiple Relaxation Time (MRT) model [40]. Recently, the central moments based collision model [41, 42] shows promising potentials in terms of numerical stability with few free parameters. Another solution is sub-grid turbulence models in which the influence of sub-grid eddies are considered as an additional eddy viscosity. In this study, the Smagorinsky sub-grid turbulence module introduced by Feng [43] is employed. The scales are divided into filtered and unresolved scales by the filtering of the LBE based on the lattice size Δx_{LBM} . The LBE can be directly solved for filtered scales. An additional relaxation time τ_a is used to represent the effect of motion at the unresolved scales [40]:

$$\tau_{total} = \tau + \tau_a, \quad (18)$$

where τ_{total} is the total relaxation time. τ_a is related to the turbulence viscosity ν_a :

$$\tau_a = \frac{3\Delta t_{LBM}}{(\Delta x_{LBM})^2} \nu_a, \quad (19)$$

with the turbulence viscosity ν_a given by

$$\nu_a = (Sc\Delta x_{LBM})^2 \hat{S}, \quad (20)$$

where Sc is the Smagorinsky constant with a typical value range between 0.1 and 0.2; and the magnitude of the filtered strain-rate tensor \hat{S} can be obtained from \tilde{Q}_{ij} - the second moment of the distribution function, i.e.,

$$\hat{S} = \frac{\sqrt{2 \sum_{i,j} \tilde{Q}_{ij} \tilde{Q}_{ij}}}{2\rho_{f0} C s^2 \tau_{total}}, \quad (21)$$

where the speed of sound $Cs = 1/\sqrt{3}$ and \tilde{Q}_{ij} is given by

$$\tilde{Q}_{ij} = \sum_{k=0}^{14} e_{ki} e_{kj} (f_k - f_k^{eq}), \quad (22)$$

where f_k and f_k^{eq} are the non-equilibrium distribution function and equilibrium distribution function, respectively.

3.3. Coupling scheme between MPM and LBM

To successfully model fluid-structure interactions, the no-penetration non-slip boundary conditions need to be imposed on the fluid-solid interface properly, the hydrodynamic forces act on solids are also required. In LBM, there mainly are two categories of boundary schemes can satisfy these requirements. Firstly, macroscopic boundary conditions where macroscopic properties are modified, such as velocity corrected immersed boundary method [9] in which the effects of boundaries are replaced by a smoothed external force field for fluid. In the second category, the distribution functions are modified directly to impose boundary conditions. Here we consider the later one since it can maintain a sharp interface and fit the kinetic nature of LBM.

The LBM nodes are divided into fluid nodes and solid nodes, the fluid nodes which are close to the solid boundary are further identified as boundary nodes (\mathbf{x}_f in Fig. 2). Since the uniform-sized mesh is used in classic LBM, the curved boundaries generally locate between boundary nodes and solid nodes. Thus, the distribution functions at boundary nodes which streamed from solid nodes are missing, the key task is to determine missing distribution functions properly.

The simplest solution is the bounce-back role where molecules depart from \mathbf{x}_f with velocity $\mathbf{e}_{i'}$ hit on wall and return back to \mathbf{x}_f with opposite discrete velocity \mathbf{e}_i . It is clear that the wall is assumed to be located at the middle point between \mathbf{x}_f and \mathbf{x}_s regardless of the actual position. This assumption leads to stair-wise boundaries which damage the second-order accuracy of LBM. Therefore, interpolated bounce-back (IBB) schemes [44] are proposed to reduce geometrical errors. The idea is to interpolate the missing distribution functions from existing ones and the interpolation weights depend on $q = |\mathbf{x}_f - \mathbf{x}_w| / |\mathbf{x}_f - \mathbf{x}_s|$. Most IBB schemes need to treat $q \leq 0.5$ and $q > 0.5$ conditions separately, Yu et al [45] proposed an unified IBB scheme. The idea is to evaluate distributions at wall $f_{i'}(\mathbf{x}_w, t + \Delta t_{LBM})$ first, then the bounce-back role is applied, the missing distributions at f after streaming $f_i(\mathbf{x}_f, t + \Delta t_{LBM})$ is interpolated between $f_i(\mathbf{x}_w, t + \Delta t_{LBM})$ and $f_i(\mathbf{x}_{ff}, t + \Delta t_{LBM})$. Yu's scheme can be summarized as:

$$f_i(\mathbf{x}_w, t + \Delta t_{LBM}) = q f_{i'}^+(\mathbf{x}_f, t) + (1 - q) f_{i'}^+(\mathbf{x}_{ff}, t) + 6 \omega_{i'} \rho_f \frac{\mathbf{e}_i \cdot \mathbf{u}_w}{C^2}, \quad (23)$$

$$f_i(\mathbf{x}_f, t + \Delta t_{LBM}) = \frac{1}{1 + q} (f_i(\mathbf{x}_w, t + \Delta t_{LBM}) + \frac{q}{1 + q} f_i(\mathbf{x}_{ff}, t + \Delta t_{LBM})), \quad (24)$$

where \mathbf{u}_w is the wall velocity. Yu's scheme does not depend on the value of q , thus it is used for the coupling scheme. When the density ratio between structure and fluid approaches to 1, partitioned coupling algorithms tend to become unstable due to the added-mass effect [6, 19, 46, 47]. In the presented model, the last term in Eq. 23 which includes \mathbf{u}_w can be interpreted as the added-mass due to the moving wall. If we consider an idealized situation as shown in Fig. 3 where a 2D fully-relaxed (equilibrium) flow with a moving wall is considered. The wall is perpendicular to the x-axis and moves with a constant velocity $\mathbf{u}_w(u_x, 0)$. The dotted black line and solid black line represent the position of wall at time t and $t + \Delta t_{LBM}$ respectively. The area of replaced fluid by the moving wall is illustrated as the shadowed area in Fig. 3. Clearly, the added-mass Δm within one time step is given as: $\Delta m = -\rho_f u_x$ by assuming $\Delta x_{LBM} = \Delta t_{LBM} = 1$. Now we consider the added-mass through the last term of Eq. 23 with D2Q9 lattice model. It only affects the distribution function f_3, f_6, f_7 as shown in Fig. 3. Thus, the added mass in the present model Δm^s is given as:

$$\Delta m^s = \sum_{i=3,6,7} 6\omega_i \rho_f \frac{\mathbf{e}_i \cdot \mathbf{u}_w}{C^2} = -\frac{6\rho_f u_x}{C^2} (\omega_1 + \omega_5 + \omega_8). \quad (25)$$

With the help of $C = \Delta x_{LBM} / \Delta t_{LBM} = 1$ and $\omega_{1,2,3,4} = 1/9, \omega_{5,6,7,8} = 1/36$ for D2Q9 lattice model, we have $\Delta m^s = -\rho_f u_x$ which is exact the same as the analytical result Δm . Similar conclusions can also be found from [48]. The modified distribution functions from Eq. 23 are latter used to calculate the hydrodynamic force acted on structures.

One drawback of having sharp solid boundaries is that solid nodes may switch to fluid nodes with no fluid information since the structure can freely move within the fluid domain. Therefore, these new fluid nodes need to be initialized with proper distribution functions. This procedure is often referred to refilling algorithm. Peng et al. [49] discussed the influence of different refilling algorithms in terms of numerical stability and accuracy, their results show that refilling may have significant contributions to the numerical noise on the flocculating hydrodynamic forces. Here, the averaged extrapolation method is used as suggested [12, 49]

$$f_i(\mathbf{x}_{new}) = \frac{1}{N_{nei}} \sum_{nei} (2f_i(\mathbf{x}_{new} + \mathbf{e}_{nei}) - f_i(\mathbf{x}_{new} + 2\mathbf{e}_{nei})), \quad (26)$$

Where \mathbf{x}_{new} is the new fluid node position, \mathbf{e}_{nei} are the discrete velocities that point from \mathbf{x}_{new} to other existing neighbor fluid nodes. Notes that the new

refilled fluid nodes are not used for extrapolation. N_{nei} is the total number of possible \mathbf{e}_{nei} (considering the first neighbor fluid nodes, excluding the ones that were solid in the previous time step). After distribution functions are refilled, the macroscopic properties like density and velocity are calculated as Eq. 17.

From fluid point view, IBB can maintain sharp fluid-solid interfaces, but it also requires accurate boundary descriptions which are missing in classical MPM due to the particle representation of structures. But with the help of additional corners, CPDI can track the geometries and have sharp boundary descriptions. The structure is discretized into tetrahedrons and the boundaries are described by triangular formed by corners. Therefore, the corners are used to determine the solid interface velocity \mathbf{u}_w which is essential for Yu's scheme. As shown in Fig. 2, the crossing point \mathbf{x}_w always lays within a triangle formed by surrounding corners. Thus \mathbf{u}_w can be interpolated from the velocity of corners under barycentric coordinates s and t :

$$\mathbf{u}_w = \mathbf{u}_{c0} + s(\mathbf{u}_{c1} - \mathbf{u}_{c0}) + t(\mathbf{u}_{c2} - \mathbf{u}_{c0}) \quad (27)$$

and the which values, alongside IBB q parameter are calculated by solving an linear system:

$$\begin{bmatrix} \Delta t_{LBM} e_{ix}, x_{c0} - x_{c1}, x_{c0} - x_{c2} \\ \Delta t_{LBM} e_{iy}, y_{c0} - y_{c1}, y_{c0} - y_{c2} \\ \Delta t_{LBM} e_{iz}, z_{c0} - z_{c1}, z_{c0} - z_{c2} \end{bmatrix} \begin{bmatrix} q \\ s \\ t \end{bmatrix} = \begin{bmatrix} x_{c0} - x_f \\ y_{c0} - y_f \\ z_{c0} - z_f \end{bmatrix} \quad (28)$$

where Δx_{LBM} is the space step of LBM, e_{ix}, e_{iy}, e_{iz} are the components of i th LBM discrete velocity that points from the fluid node \mathbf{x}_f to solid node \mathbf{x}_s . The corner position \mathbf{x}_c and velocity \mathbf{u}_c are calculated as:

$$\begin{aligned} \mathbf{u}_c^{t+\Delta t_{MPM}} &= \sum_I S_I(\mathbf{x}_c^t) \mathbf{u}_I^{t+\Delta t_{MPM}} \\ \mathbf{x}_c^{t+\Delta t_{MPM}} &= \mathbf{x}_c^t + \mathbf{u}_c^{t+\Delta t_{MPM}} \Delta t_{MPM} \end{aligned} \quad (29)$$

The material point position is then updated by averaging the surrounding corner positions:

$$\mathbf{x}_p = \frac{1}{4} \sum_c \mathbf{x}_c \quad (30)$$

The influence of solid structure on the fluid is modelled by the above no-penetration non-slip boundary conditions, the structure interacts with fluid

though the hydrodynamic forces. The hydrodynamic forces \mathbf{f}_s^h appear in Eq. 2 as external forces. Accurate and efficient calculation of \mathbf{f}_s^h is essential for a successful coupling scheme. One widely used scheme is the momentum exchange method [50], where the hydrodynamic forces can be calculated as a sum of all the momentum exchanges along with every discrete velocity that collides with solid walls. The momentum exchange method is extensively used for fluid-particle interactions. However, it suffers from numerical noises which introduce extreme flocculating hydrodynamic forces [49]. Wen et al. [51] shows that the original momentum exchange method does obey the Galilean invariant principle. They further proposed a Galilean invariant momentum exchange method which relief numerical noises considerable. Therefore, the Galilean invariant momentum exchange method is adapted in this work, the momentum exchange along \mathbf{e}_i is given:

$$\mathbf{f}_s^{h,i}(\mathbf{x}_w, t) = (\mathbf{e}_i - \mathbf{u}_w) f_i(\mathbf{x}_f, t) - (\mathbf{e}_{i'} - \mathbf{u}_w) f_{i'}(\mathbf{x}_f, t) - 2\rho_0 w_i \mathbf{e}_i \quad (31)$$

Where i represents all the directions of missing distribution functions after streaming, i' is the opposite direction of i . Compared with the original momentum exchange method, \mathbf{e}_i is shifted by the solid velocity. Since the pressure fluctuation is considered in LBM instead of the total pressure, the last term $2\rho_0 w_i \mathbf{e}_i$ refers to the influence of the reference pressure [12]. Since the missing distribution functions are calculated by Eq. 23 in which the added-mass is represented by the last term of Eq. 23, therefore, the added-mass effect on structures is take into account through Eq. 31. Note that $\mathbf{f}_s^{h,i}$ cannot be directly used for MPM since it acts at \mathbf{x}_w . Therefore, it is distributed to surrounding corners as a function of the barycentric coordinates obtained beforehand:

$$\begin{aligned} \mathbf{f}_s^{h,i}(\mathbf{x}_{c0}, t) &= (1 - s - t) \mathbf{f}_s^{h,i}(\mathbf{x}_w, t) \\ \mathbf{f}_s^{h,i}(\mathbf{x}_{c1}, t) &= s \mathbf{f}_s^{h,i}(\mathbf{x}_w, t) \\ \mathbf{f}_s^{h,i}(\mathbf{x}_{c2}, t) &= t \mathbf{f}_s^{h,i}(\mathbf{x}_w, t) \end{aligned} \quad (32)$$

The hydrodynamic force acts at corners can be obtained by:

$$\mathbf{f}_s^h(\mathbf{x}_c, t) = \sum_l \mathbf{f}_s^{h,l}(\mathbf{x}_c, t) \quad (33)$$

Where the set l includes all the directions of missing distribution functions. Finally, the nodal hydrodynamic force in Eq. 2 is interpolated from corners:

$$\mathbf{f}_s^h(\mathbf{x}_I, t) = \sum_c S_I(\mathbf{x}_c) \mathbf{f}_s^h(\mathbf{x}_c, t) \quad (34)$$

4. Validation

4.1. Validation of MPM structure solver: Elastic beam

To validate the MPM structure solver, cantilever beam simulations are conducted and compared with Euler's beam theory. The dimension is a length of $L = 100$ mm and a square cross-section of side $S = 20$ mm. The material properties are given as: Density $\rho_s = 1030$ kg/m³, Young's modulus $E = 1.23 \times 10^6$ pa and Poisson ratio $\nu_s = 0.3$. The left end of the beam is fixed and the right end is free to deform under loads as illustrated in Fig. 4. A force F is applied at the right end of the beam, which is achieved by distributing it uniformly over the corner points at the end of the beam. The force linearly increases from 0 at the beginning to the maximum value and stays at the desired value for numerical stability consideration. The beam is discretized into material points and the space step of the background mesh is determined as $\Delta x_{MPM} = \beta L_c$ where β is the resolution ratio and L_c is a characteristic length of the particle domain. The maximum dimension of tetrahedron elements is chosen as L_c and $\beta = 1$. The time step is given as $\Delta t_{MPM} = L/(n_x C_s^{MPM})$ where n_x is the approximated number of material points along x-axis. The MPM solid speed of sound is calculated as $C_s^{MPM} = \sqrt{E/\rho_s}$. The damping coefficient η_{damp} is set to 1 s^{-1} to disperse kinetic energy and help the system reaches the equilibrium state.

By keeping S/L and deformation small, Euler's beam theory can be used to determine the deviation w of the cantilever's middle plane along the x coordinate as:

$$w(x) = \frac{Fx^2(3L - x)}{6EI} \quad (35)$$

where $I = S^4/12$ is the second area moment of the square cross-section. The simulated displacement configuration matches well with Euler's beam theory for $F = 1$ N as shown in Fig. 5. The model is further evaluated by varying loading force F from 1×10^{-3} to 1 N. Maximum displacements are plotted against loading forces in Fig. 6. A good agreement is found between simulations and the analytical solution (Eq. 35).

4.2. Validation of LBM flow solver: flow around a circle

Flow around an obstacle is simulated to validate the LBM fluid solver. Using dimensional analysis, two dimensionless numbers: Reynolds number Re and drag coefficient C_d can be defined as:

$$Re = \frac{\bar{u}_x D_c}{\nu_f} \quad (36)$$

$$C_d = \frac{8F_x}{\rho_f \bar{u}_x^2 \pi D_c^2} \quad (37)$$

where \bar{u}_x is the x component of averaged velocity over the fluid domain. The characteristic length D_c is defined as the circle diameter. ρ_f and ν_f are the fluid density and kinematic viscosity. F_x is the x component of the total hydrodynamic force acted on the obstacle. According to Buckingham π theorem, C_d must be a function of Re .

A circle obstacle is used as the first example to demonstrate the applicability of the LBM fluid solver for turbulence flows with the help of LES sub-grid scheme. The circle with a diameter of 42 cells is placed in the middle of a 2100×2100 cells domain as shown in Fig. 7. The circle diameter is chosen as the characteristic length D_c . Velocity boundary conditions are applied on the left and right with a velocity equal to 0.1 in lattice units. The Re is controlled by varying the viscosity ν_f . F_x is calculated by summing momentum exchanges over the solid boundary, more details can be found in [52]. The value for F_x is taken as a time average to eliminate the fluctuations that appear at high Re values due to the presence of eddies. C_d as a function of Re is plotted in Fig. 8. Even for very high Re , the LES scheme produces accurate and stable results when compared with experimental results.

4.3. Validation of MPM-LBM force coupling: flow around a cube

The second validation is flows around a 3D cube. Since the goal is to couple MPM with LBM, thus the cube obstacle is described by MPM particles with no deformation and zero velocities. The side length of the cube is $L_{cube} = 1.45\text{m}$ and it is discretized into 6 tetrahedral material points with their associated tetrahedron elements. The fluid domain size is $24.1\text{m} \times 6.1\text{m} \times 6.1\text{m}$. Fluid density ρ_f and kinetic viscosity ν_f are 1000 kg/m^3 and $2.0803 \times 10^{-6} \text{ m}^2 \cdot \text{s}$ accordingly. The cube is placed at the center of the fluid domain ($12.05\text{m} \times 3.05\text{m} \times 3.05\text{m}$) as shown in Fig. 9. Since the ratio between cube size and domain width is fairly small, periodic boundary conditions are applied to all six domain boundaries. The space and time step are chosen as $\Delta x_{LBM} = 0.1\text{m}$ and $\Delta t_{LBM} = \Delta t_{MPM} = 0.2\text{s}$. The fluid field is initialized with zero velocity and the fluid is driven by a body force. The characteristic length is given as $D_c = 1.2407 \cdot L_{cube}$. During simulations, Re increase with time due to the constant body force. The relation between C_d and Re can only be expressed analytically for sphere shape under the limitation of $Re \ll 1$. Thus, many empirical corrections are developed for non-spherical

shapes and high Re . The formula proposed by Swamee and Ojha [53] is used as comparisons:

$$C_d = \frac{128Re^{-0.8}}{1 + 4.5\beta_s^{0.35}} \quad (38)$$

where the shape factor $\beta_s = c/\sqrt{ab}$ and $a = b = c = 1$ for cube. Two simulations are conducted with different body force values: 2.5×10^{-5} and $2.5 \times 10^{-5} \text{m/s}^2$. This low body force value ensures a broad range of low Re values with corresponding C_d in a single simulation run. As shown in Fig. 10, good agreements are found between simulated C_d and the prediction from Eq. 38 regardless of different body forces, which implies that the LBM fluid solver can be used to interstage flow problems with large range of Re .

4.4. Validation of MPM-LBM coupling: a flexible plate deformation in shear flow

Finally, the MPM-LBM coupling scheme is validated by simulating a classical FSI problem: a flexible plate deforms in a shear flow. As illustrated in Fig. 11, the elastic plate with length $l = 0.1\text{m}$, width $k = 0.02\text{m}$ and thickness b is immersed in the flow vertically and attached to the middle of the bottom. Rest part of the plate can freely move, thus the plate bends under shear flows. The material properties of the plate are given as: Density $\rho_s = 1030\text{kg/m}^3$ Young's modulus $E = 1.23 \times 10^6 \text{ pa}$ and Poisson ratio $\nu_s = 0.3$. The domain size is fixed to $0.2\text{m} \times 0.5\text{m} \times 0.5\text{m}$.

The velocity boundary condition is applied to the inlet and zero velocity gradient boundary condition for the outlet (see Fig. 11). To mimic the experimental setup of Bano et al. [54], the top boundary is set to be free slipping. Boundaries normal to the y-axis are periodic and the bottom boundary is solid wall. The fluid field is initialized with zero velocity and the velocity profile of inlet is given as:

$$v(z) = v_{max} \left(1 - \frac{(z - L)^2}{L^2} \right) \quad (39)$$

where z is the height of cells and the domain height $L = 0.5\text{m}$. The top velocity v_{max} is determined by Reynolds number as: $v_{max} = 1.5Re\nu_f/L$. Fluid density ρ_f and kinetic viscosity ν_f are 1220 kg/m^3 and $8.2 \times 10^{-4} \text{m}^2 \cdot \text{s}$ accordingly. During simulations, v_{max} linearly increases from zero to the desired value to avoid a sharp velocity gradient.

To meet the numerical stable conditions for both MPM and LBM, the time step is determined as $\Delta t_{LBM} = \Delta t_{MPM} = l/(n_z C_s^{MPM})$ where n_z is the approximated number of material points along z-axis which controls the MPM particle resolution. Here, $n_z = 50$ is used. The MPM solid speed of sound is calculated as $C_s^{MPM} = \sqrt{E/\rho_s}$. Same time step is applied to both MPM and LBM since the coupling scheme requires information exchange at the same time frame. Although both MPM and LBM use Cartesian grids, they do not need to coincide and in fact they do not match in any of the cases presented here. The mesh resolution of the MPM grid is determined as $\Delta x_{MPM} = \beta L_c$ where L_c is a characteristic length of the particle domain and the maximum dimension of tetrahedron elements is chosen as L_c as explained before. β is a parameter that controls the ratio between MPM mesh resolution and particle resolution. The LBM space step is given as $\Delta x_{LBM} = 5 \times 10^{-4}\text{m}$.

Two types of plates with $b = 0.005$ and 0.01m are simulated and compared with the experimental results from Bano et al. [54] under the same conditions. The Reynolds number $Re = 9$ is used, the Mach number is given as $Ma = 0.00312$ and the relaxation time $\tau = 1.541762$. Due to the low Reynolds number, the plate can reach a steady state when the hydrodynamic force balanced with the elastic stress. It is found that β has a significant influence on the model accuracy, with $\beta = 1.5$, the simulated steady-state plate configurations show great agreements with experimental results as seen in Fig. 12.

5. Numerical examples

An important feature of the present model is that it can handle turbulence flows with the help of LES sub-grid model. To demonstrate its capability for high Re applications, simulations of a flexible plate deforms in a shear flow under high Re are conducted. The simulation setup is same as in Sec. 4.4 with plate width $b = 0.005\text{m}$. v_{max} is fixed (same value as in Sec. 4.4) due to the low Mach number requirement of LBM. Re is controlled by varying the fluid viscosity. Seven values of Re are simulated: $Re = 1, 10, 100, 1 \times 10^3, 1 \times 10^4, 1 \times 10^5$ and 1×10^6 . The relaxation time is given as $\tau = 9.875858, 1.437586, 0.5937586, 0.5093759, 0.5009376, 0.5000938$ and 0.5000094 accordingly. With the help of LES sub-grid model, simulations are numerically stable even when τ approaches to 0.5.

The averaged position of the plate top layer is monitored. Time evolutions of the plate deflection along x-axis (δ_x) are plotted in Fig. 13 where deflections are rescaled by L . Three stages can be identified regardless of Re : δ_x increases with time linearly at the first stage, identical increase rates are found for all Re . Rapid decreases are observed after δ_x reach to the maximum value (expect for $Re = 1$). At the third stage, the time-averaged δ_x stay as a constant since the plate reaches the equilibrium configuration. Boundaries between stages are insensitive to Re . But Re has a significant influence on the maximum and equilibrium value of δ_x . For $Re < 1 \times 10^3$, δ_x does not change with time during the third stage. It is worth to point out that equilibrium δ_x does not monotonic increase with Re . For example, larger equilibrium δ_x is found with $Re = 1$ comparing with $Re = 100$. For $Re > 1 \times 10^3$, equilibrium δ_x barely change with Re and δ_x flocculates around the equilibrium value. Periodic patterns of δ_x are also found and the magnitude and frequency are independent to Re . The deflection along z-axis (δ_z) are also plotted in Fig. 13. Overall, the patterns of δ_z are very similar as δ_x , but stronger oscillations of δ_z are founded when $Re > 1 \times 10^3$. Fig. 15 and 16 show snapshots of the plate configuration and fluid velocity field for $Re = 1$ and 1×10^3 . The truculent flows at $Re = 1 \times 10^3$ are mainly responsible to the oscillations of plate.

The last example is a deformable fish (Fig. 17) swings in flows. Fig. 18 shows interactions between the fish and surrounding fluid. Periodic boundaries are applied along x-xis and rest boundaries are solid walls. The flow is driven by a constant body force, 1/3 of the fish is fixed and rest are free to move. It can be found that the fishtail starts to swing which demonstrates the capability of the proposed model on handling FSI problems with complex geometry obtained from CAD meshes. Videos of this simulation are attached as supplementary material.

6. Conclusion

In this paper, we introduced a 3D numerical scheme to simulate FSI problems with large deformation under high Reynolds number. Using interpolated bounce back scheme and momentum exchange method, the efficiency of LBM on solving flows and the capability of MPM on handling large deformations are integrated together. The recently developed CDPI scheme of MPM ensures sharp descriptions of solid boundaries. The LBM is enhanced

by LES sub-grid model for turbulence flows. Implementations of MPM, LBM and the coupling scheme are presented in detail.

The MPM structure solver is validated by comparing with Euler beam theory with great agreements. Then the LBM fluid solver is tested for fluid round circle and cube obstacles under a large range of Re . It is found that the fluid solver can handle high Re simulations with decent accuracy. The coupled model is then compared with experiments of a deformable plate under shear flow. The simulated plate equilibrium configurations match well with experimental observations for different plate dimensions.

To demonstrate the capability of the model for high Re applications, the plate deformations under shear flows are simulated with Re from 1 to 1×10^6 . Significant differences in structural response are found for various Re . An equilibrium state can be reached for low Re , where periodic oscillations are founded at high Re . The model is then applied to simulate fish motions in the flow which clearly shows that the model can handle complex structure geometries.

In conclusion, the presented results demonstrate the potential of the model as a powerful numerical tool to investigate FSI problems, particularly for large deformations, complex structure geometries and high Re situations which can be found in many engineering and science disciplines.

Acknowledgement

We gratefully acknowledge the funding from the Westlake Education Foundation, the Belt and Road Special Foundation of the State Key Laboratory of Hydrology-Water Resources and Hydraulic Engineering (2019491511), Natural Science Foundation of Zhejiang Province (LHZ21E090002). The presented simulations were conducted based on the Mechsys open source library (<http://mechsys.nongnu.org>) and using computational resources from the Westlake University Supercomputer Center.

References

- [1] F.-B. Tian, H. Dai, H. Luo, J. F. Doyle, B. Rousseau, Fluid–structure interaction involving large deformations: 3d simulations and applications to biological systems, *Journal of computational physics* 258 (2014) 451–469.

- [2] X. Wang, X. Zeng, J. Li, X. Yang, H. Wang, A review on recent advancements of substructures for offshore wind turbines, *Energy conversion and management* 158 (2018) 103–119.
- [3] M. Bergmann, A. Iollo, Modeling and simulation of fish-like swimming, *Journal of Computational Physics* 230 (2) (2011) 329–348.
- [4] A. Alizadeh, A. Dadvand, Effects of deformability of rbc on their dynamics and blood flow passing through a stenosed microvessel: an immersed boundary-lattice boltzmann approach, *Theoretical and Computational Fluid Dynamics* 32 (1) (2018) 91–107.
- [5] Y. T. Nguyen Edalgo, A. L. Zornes, A. N. Ford Versypt, A hybrid discrete–continuous model of metastatic cancer cell migration through a remodeling extracellular matrix, *AIChE Journal* 65 (9) (2019) e16671.
- [6] A. De Rosis, G. Falcucci, S. Ubertini, F. Ubertini, A coupled lattice boltzmann-finite element approach for two-dimensional fluid–structure interaction, *Computers & Fluids* 86 (2013) 558–568.
- [7] C. Hesch, A. Gil, A. A. Carreno, J. Bonet, P. Betsch, A mortar approach for fluid–structure interaction problems: Immersed strategies for deformable and rigid bodies, *Computer Methods in Applied Mechanics and Engineering* 278 (2014) 853–882.
- [8] A. Gilmanov, T. B. Le, F. Sotiropoulos, A numerical approach for simulating fluid structure interaction of flexible thin shells undergoing arbitrarily large deformations in complex domains, *Journal of computational physics* 300 (2015) 814–843.
- [9] J. Wu, J. Wu, J. Zhan, N. Zhao, T. Wang, A robust immersed boundary-lattice boltzmann method for simulation of fluid-structure interaction problems, *Communications in Computational Physics* 20 (1) (2016) 156–178.
- [10] X. Niu, C. Shu, Y. Chew, Y. Peng, A momentum exchange-based immersed boundary-lattice boltzmann method for simulating incompressible viscous flows, *Physics Letters A* 354 (3) (2006) 173–182.

- [11] J. Lee, D. You, An implicit ghost-cell immersed boundary method for simulations of moving body problems with control of spurious force oscillations, *Journal of Computational Physics* 233 (2013) 295–314.
- [12] Y. Liu, H. Ye, H. Zhang, Y. Zheng, Coupling lattice boltzmann and material point method for fluid-solid interaction problems involving massive deformation, *International Journal for Numerical Methods in Engineering* 121 (24) (2020) 5546–5567.
- [13] T. Richter, T. Wick, Finite elements for fluid–structure interaction in ale and fully eulerian coordinates, *Computer Methods in Applied Mechanics and Engineering* 199 (41-44) (2010) 2633–2642.
- [14] S. Basting, A. Quaini, S. Čanić, R. Glowinski, Extended ale method for fluid–structure interaction problems with large structural displacements, *Journal of Computational Physics* 331 (2017) 312–336.
- [15] C. S. Peskin, The immersed boundary method, *Acta numerica* 11 (2002) 479–517.
- [16] W.-Q. Wang, Y. Yan, G. Liu, An ib-lbm implementation for fluid-solid interactions with an mls approximation for implicit coupling, *Applied Mathematical Modelling* 62 (2018) 638–653.
- [17] R. Mittal, H. Dong, M. Bozkurttas, F. Najjar, A. Vargas, A. Von Loebbecke, A versatile sharp interface immersed boundary method for incompressible flows with complex boundaries, *Journal of computational physics* 227 (10) (2008) 4825–4852.
- [18] J. H. Seo, R. Mittal, A sharp-interface immersed boundary method with improved mass conservation and reduced spurious pressure oscillations, *Journal of computational physics* 230 (19) (2011) 7347–7363.
- [19] E. Van Brummelen, Partitioned iterative solution methods for fluid–structure interaction, *International Journal for Numerical Methods in Fluids* 65 (1-3) (2011) 3–27.
- [20] C.-L. Gong, Z. Fang, G. Chen, Numerical investigation of nonlinear fluid–structure interaction dynamic behaviors under a general immersed boundary-lattice boltzmann-finite element method, *International Journal of Modern Physics C* 29 (04) (2018) 1850038.

- [21] R. Van der Sman, Galilean invariant lattice boltzmann scheme for natural convection on square and rectangular lattices, *Physical Review E* 74 (2) (2006) 026705.
- [22] P. Zhang, S. Galindo-Torres, H. Tang, G. Jin, A. Scheuermann, L. Li, Lattice boltzmann simulations of settling behaviors of irregularly shaped particles, *Physical Review E* 93 (6) (2016) 062612.
- [23] P. Zhang, S. Galindo-Torres, H. Tang, G. Jin, A. Scheuermann, L. Li, An efficient discrete element lattice boltzmann model for simulation of particle-fluid, particle-particle interactions, *Computers & Fluids* 147 (2017) 63–71.
- [24] S. Galindo-Torres, A coupled discrete element lattice boltzmann method for the simulation of fluid–solid interaction with particles of general shapes, *Computer Methods in Applied Mechanics and Engineering* 265 (2013) 107–119.
- [25] S. Galindo-Torres, D. Pedroso, D. Williams, L. Li, Breaking processes in three-dimensional bonded granular materials with general shapes, *Computer Physics Communications* 183 (2) (2012) 266–277.
- [26] Y. Chen, G. Jin, P. Zhang, S. Galindo-Torres, A. Scheuermann, L. Li, An efficient framework for particle-fluid interaction using discrete element lattice boltzmann method: coupling scheme and periodic boundary condition, *Computers & Fluids* (2020) 104613.
- [27] T. Krüger, F. Varnik, D. Raabe, Efficient and accurate simulations of deformable particles immersed in a fluid using a combined immersed boundary lattice boltzmann finite element method, *Computers & Mathematics with Applications* 61 (12) (2011) 3485–3505.
- [28] J. R. Clausen, D. A. Reasor Jr, C. K. Aidun, Parallel performance of a lattice-boltzmann/finite element cellular blood flow solver on the ibm blue gene/p architecture, *Computer physics communications* 181 (6) (2010) 1013–1020.
- [29] D. Tskhakaya, K. Matyash, R. Schneider, F. Taccogna, The particle-in-cell method, *Contributions to Plasma Physics* 47 (8-9) (2007) 563–594.

- [30] D. Sulsky, S.-J. Zhou, H. L. Schreyer, Application of a particle-in-cell method to solid mechanics, *Computer physics communications* 87 (1-2) (1995) 236–252.
- [31] J. J. Monaghan, Smoothed particle hydrodynamics, *Annual review of astronomy and astrophysics* 30 (1) (1992) 543–574.
- [32] T. Belytschko, Y. Y. Lu, L. Gu, Element-free galerkin methods, *International journal for numerical methods in engineering* 37 (2) (1994) 229–256.
- [33] V. P. Nguyen, C. T. Nguyen, T. Rabczuk, S. Natarajan, On a family of convected particle domain interpolations in the material point method, *Finite Elements in Analysis and Design* 126 (2017) 50–64.
- [34] S. G. Bardenhagen, E. M. Kober, The generalized interpolation material point method, *Computer Modeling in Engineering and Sciences* 5 (6) (2004) 477–496.
- [35] A. Sadeghirad, R. M. Brannon, J. Burghardt, A convected particle domain interpolation technique to extend applicability of the material point method for problems involving massive deformations, *International Journal for numerical methods in Engineering* 86 (12) (2011) 1435–1456.
- [36] S. Galindo-Torres, A. Scheuermann, L. Li, Numerical study on the permeability in a tensorial form for laminar flow in anisotropic porous media, *Physical Review E* 86 (4) (2012) 046306.
- [37] S. Galindo-Torres, A. Scheuermann, L. Li, D. Pedroso, D. Williams, A lattice boltzmann model for studying transient effects during imbibition–drainage cycles in unsaturated soils, *Computer Physics Communications* 184 (4) (2013) 1086–1093.
- [38] Z. Guo, C. Zheng, B. Shi, Discrete lattice effects on the forcing term in the lattice boltzmann method, *Physical review E* 65 (4) (2002) 046308.
- [39] A. Mohamad, *Lattice Boltzmann Method*, Vol. 70, Springer, 2011.
- [40] H. Yu, S. S. Girimaji, L.-S. Luo, Dns and les of decaying isotropic turbulence with and without frame rotation using lattice boltzmann method, *Journal of Computational Physics* 209 (2) (2005) 599–616.

- [41] A. De Rosis, Non-orthogonal central moments relaxing to a discrete equilibrium: A d2q9 lattice boltzmann model, *EPL (Europhysics Letters)* 116 (4) (2017) 44003.
- [42] A. De Rosis, E. L  v  que, Central-moment lattice boltzmann schemes with fixed and moving immersed boundaries, *Computers & Mathematics with Applications* 72 (6) (2016) 1616–1628.
- [43] Y. Feng, K. Han, D. Owen, Coupled lattice boltzmann method and discrete element modelling of particle transport in turbulent fluid flows: Computational issues, *International Journal for Numerical Methods in Engineering* 72 (9) (2007) 1111–1134.
- [44] M. Bouzidi, M. Firdaouss, P. Lallemand, Momentum transfer of a boltzmann-lattice fluid with boundaries, *Physics of fluids* 13 (11) (2001) 3452–3459.
- [45] D. Yu, R. Mei, L.-S. Luo, W. Shyy, Viscous flow computations with the method of lattice boltzmann equation, *Progress in Aerospace Sciences* 39 (5) (2003) 329–367.
- [46] E. H. van Brummelen, Added mass effects of compressible and incompressible flows in fluid-structure interaction, *Journal of Applied mechanics* 76 (2) (2009).
- [47] P. Causin, J.-F. Gerbeau, F. Nobile, Added-mass effect in the design of partitioned algorithms for fluid–structure problems, *Computer methods in applied mechanics and engineering* 194 (42-44) (2005) 4506–4527.
- [48] Y. Chen, Q. Cai, Z. Xia, M. Wang, S. Chen, Momentum-exchange method in lattice boltzmann simulations of particle-fluid interactions, *Physical Review E* 88 (1) (2013) 013303.
- [49] C. Peng, Y. Teng, B. Hwang, Z. Guo, L.-P. Wang, Implementation issues and benchmarking of lattice boltzmann method for moving rigid particle simulations in a viscous flow, *Computers & Mathematics with Applications* 72 (2) (2016) 349–374.
- [50] A. J. Ladd, Numerical simulations of particulate suspensions via a discretized boltzmann equation. part 1. theoretical foundation, *Journal of fluid mechanics* 271 (1994) 285–309.

- [51] B. Wen, C. Zhang, Y. Tu, C. Wang, H. Fang, Galilean invariant fluid–solid interfacial dynamics in lattice boltzmann simulations, *Journal of Computational Physics* 266 (2014) 161–170.
- [52] S. Galindo-Torres, S. Palma, S. Quintero, A. Scheuermann, X. Zhang, K. Krabbenhoft, M. Ruest, D. Finn, An airblast hazard simulation engine for block caving sites, *International Journal of Rock Mechanics and Mining Sciences* 107 (2018) 31–38.
- [53] P. K. Swamee, C. S. P. Ojha, Drag coefficient and fall velocity of non-spherical particles, *Journal of Hydraulic Engineering* 117 (5) (1991) 660–667.
- [54] T. Bano, F. Hegner, M. Heinrich, R. Schwarze, Investigation of fluid-structure interaction induced bending for elastic flaps in a cross flow, *Applied Sciences* 10 (18) (2020) 6177.

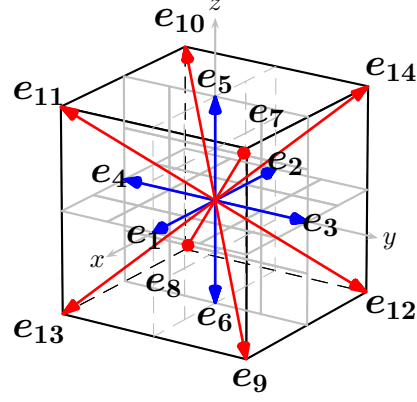


Figure 1: Discrete velocity vectors for D3Q15 [24].

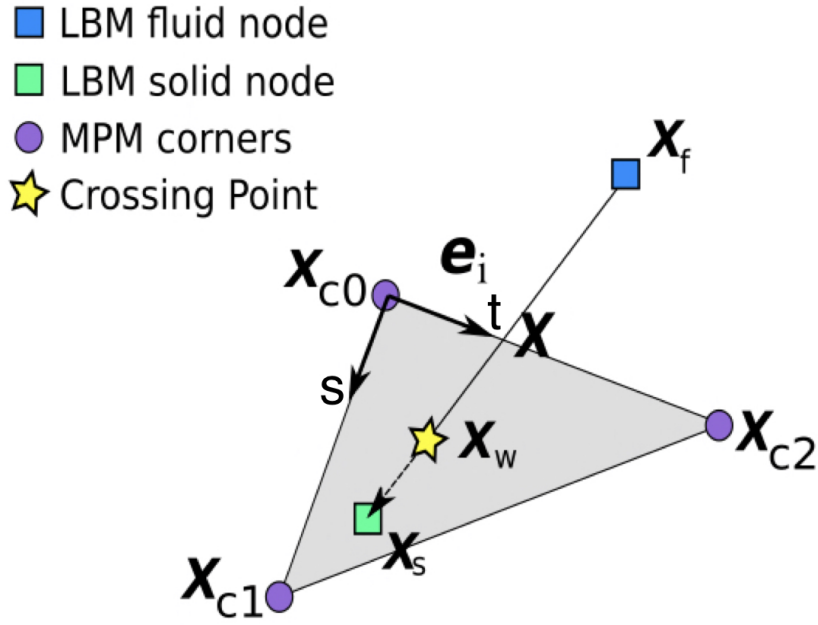


Figure 2: Schematic of the interpolated bounce back rule at the fluid-structure interface, where “s” for the closest solid node, “w” for wall, “f” for the boundary node, “ff” for the neighbouring fluid node of “f”.

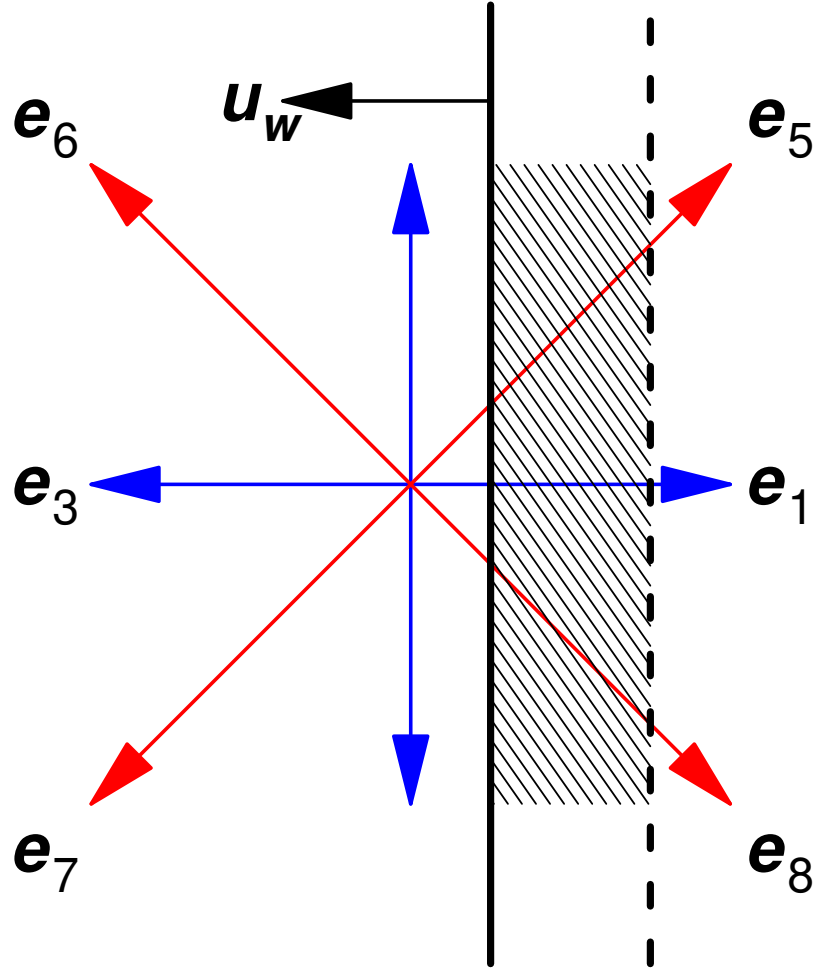


Figure 3: The dotted black line and solid black line represent the position of wall at time t and $t + \Delta t$ respectively. The shadowed area represent the area of replaced fluid due to the moving wall.

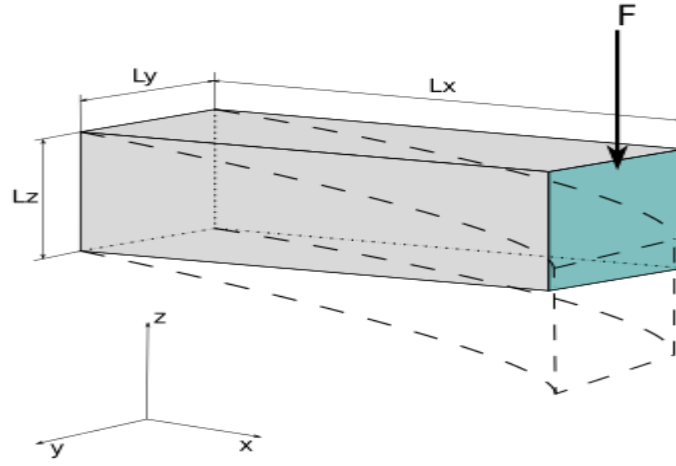


Figure 4: Elastic beam simulation setup.

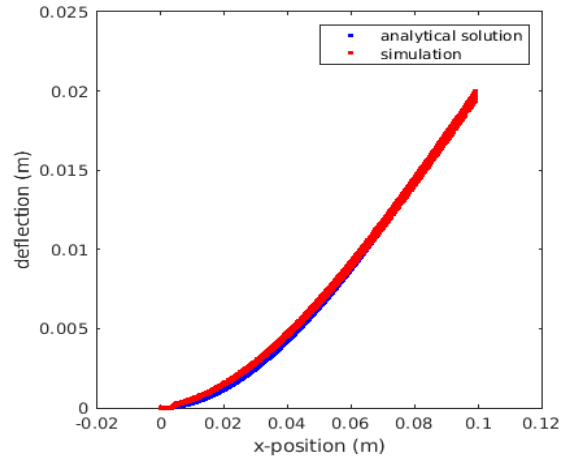


Figure 5: Comparison of displacement configuration between MPM simulation and Euler beam theory with 1.0N loading.

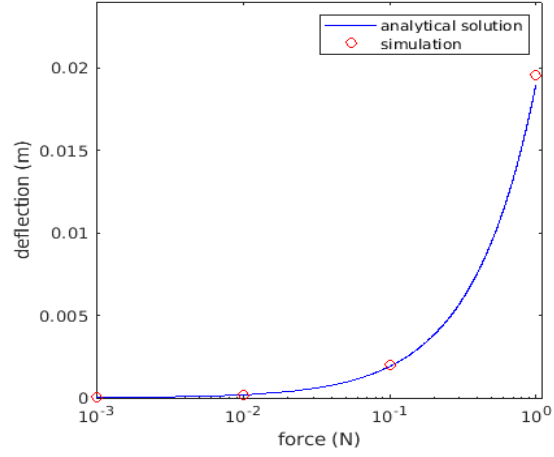


Figure 6: Maximum deflection as a function of the loading force.

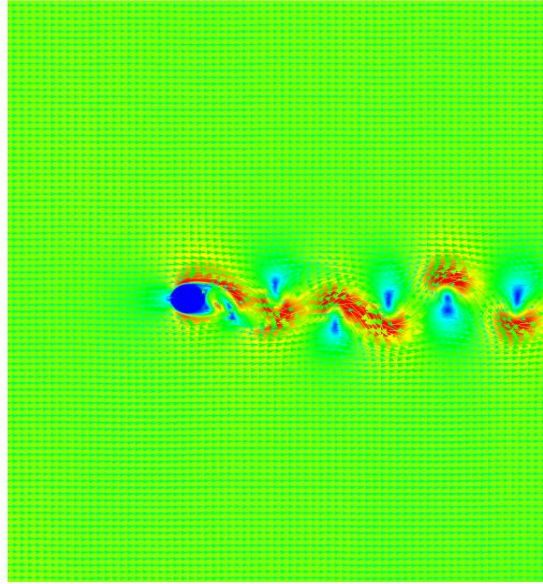


Figure 7: Snapshot of the drag coefficient simulation for $Re = 1000$.

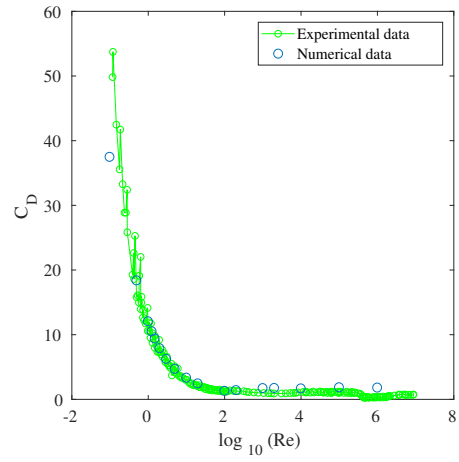


Figure 8: Obtained value for the drag coefficient C_d of a circle as a function of Re .

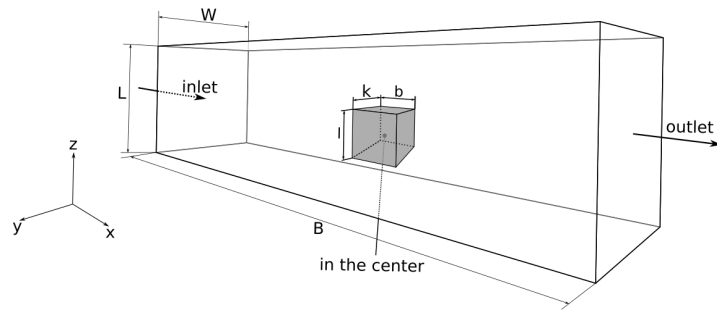


Figure 9: Simulation setup for flows around a cube.

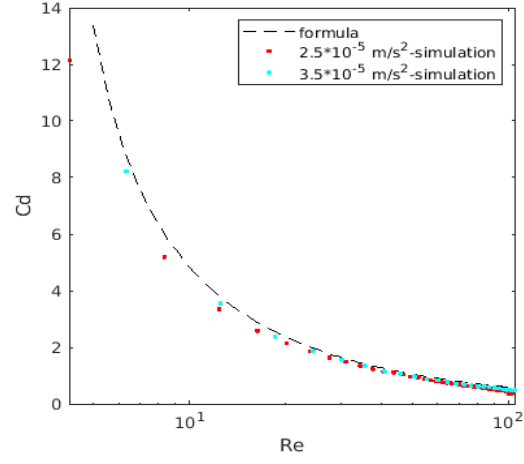


Figure 10: The simulated drag coefficient C_d of a cube as a function of Re .

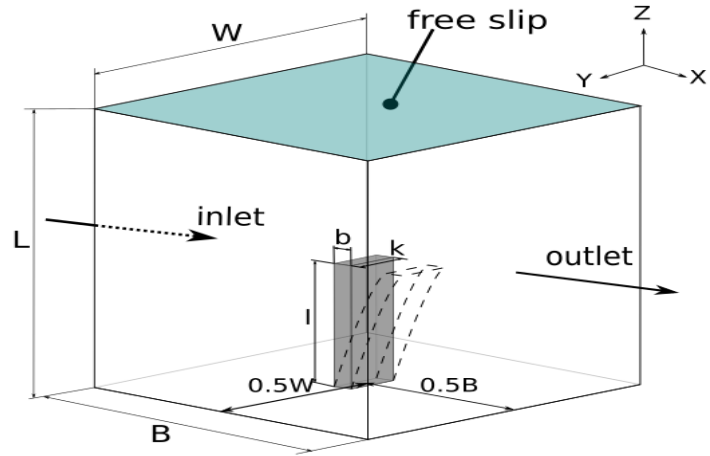


Figure 11: Simulation setup for a flexible plate deformation in shear flow.

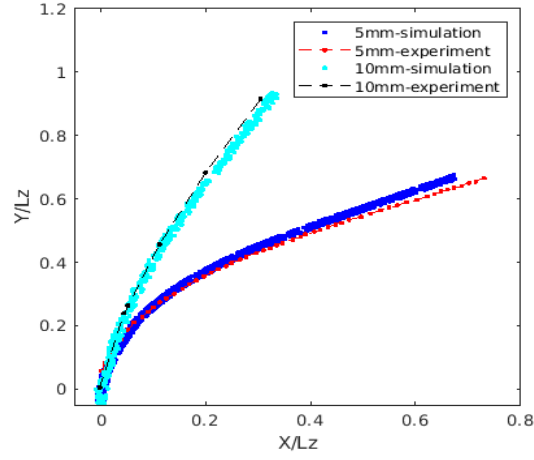


Figure 12: Steady plate configurations compared with experiments [54] with different thicknesses, $Re = 9$.

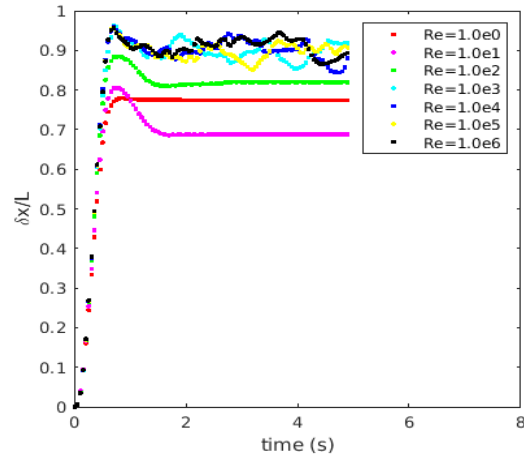


Figure 13: The plate deflection along x-axis δ_x as a function of time and Re .

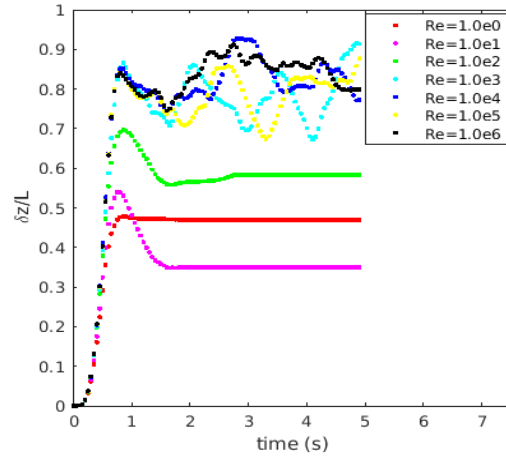


Figure 14: The plate deflection along z-axis δ_z as a function of time and Re .

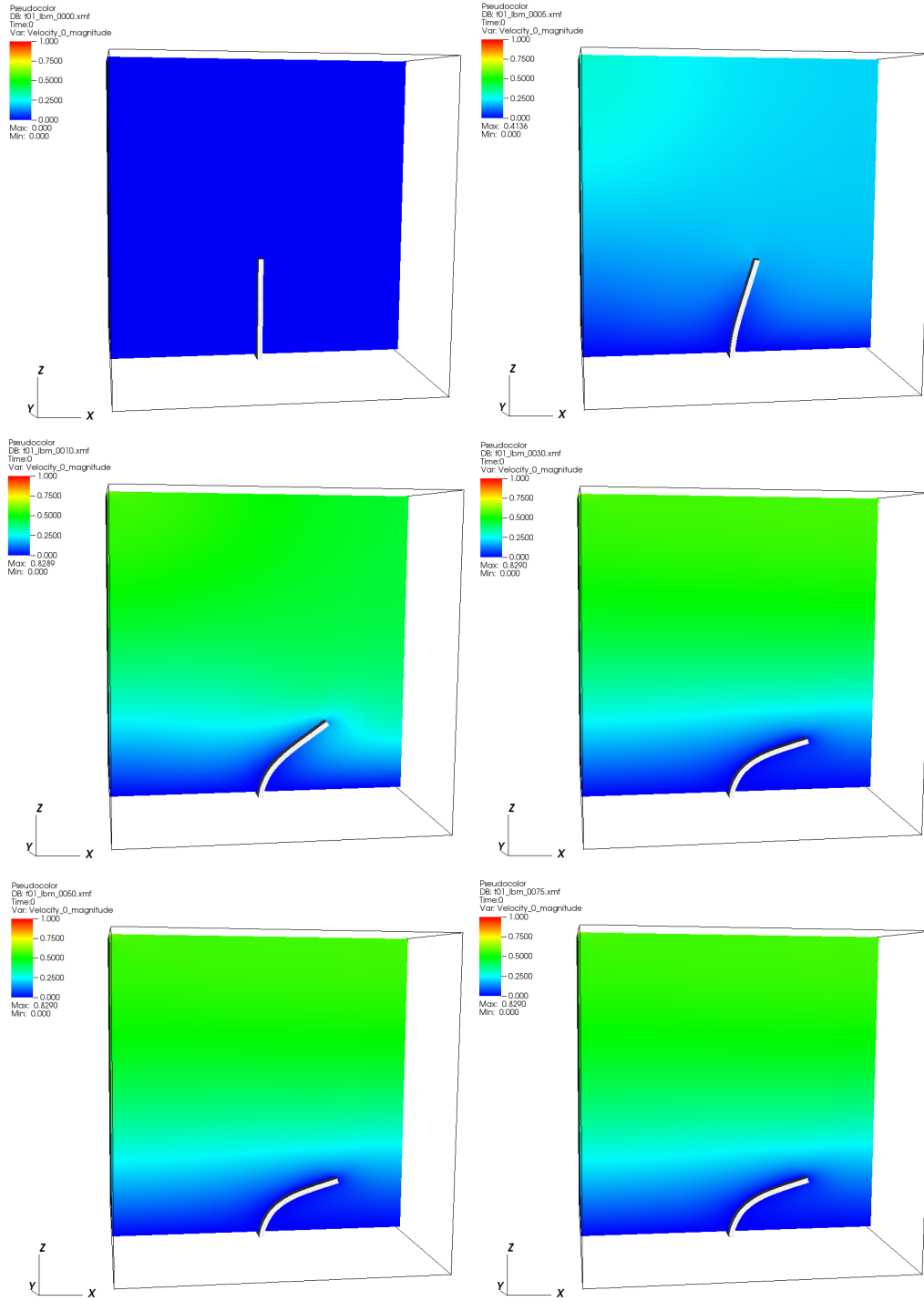


Figure 15: Snapshot of the plate configuration and fluid velocity field at $Re = 1$.

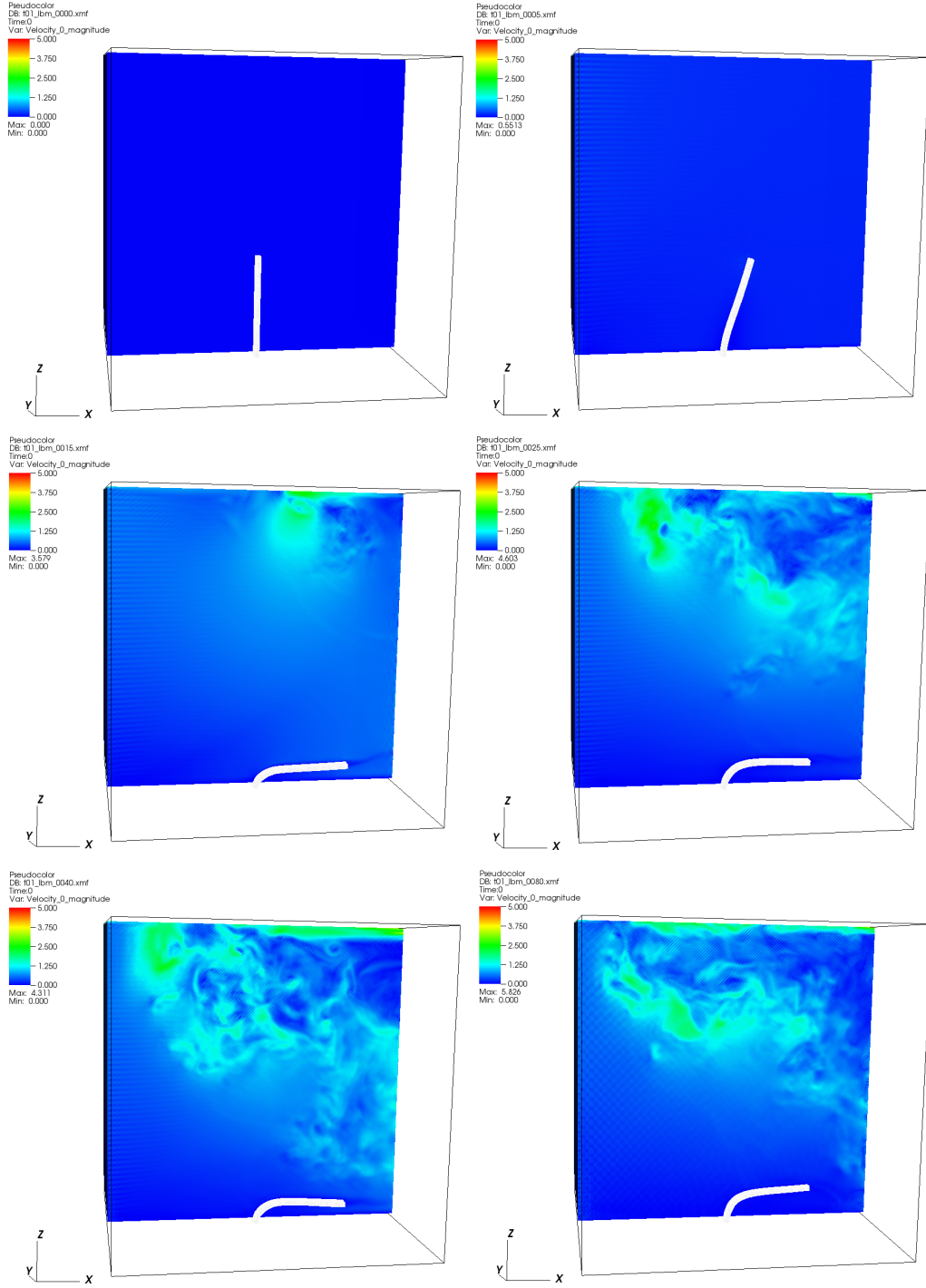


Figure 16: Snapshot of the plate configuration and fluid velocity field at $Re = 1 \times 10^3$.

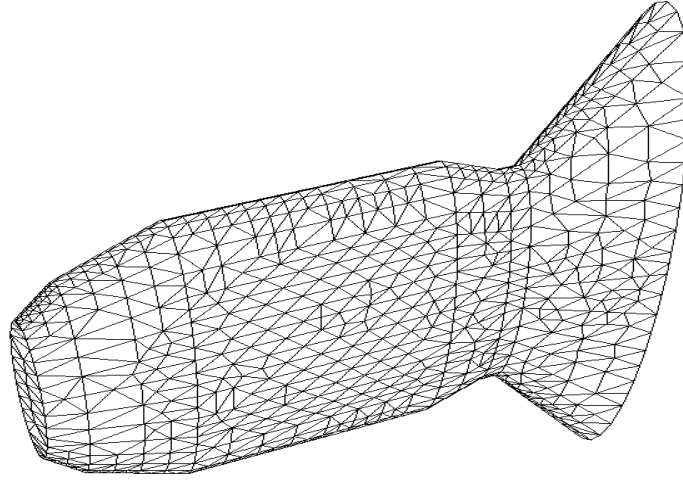


Figure 17: A tetrahedron mesh for CPDI to describe a fish.

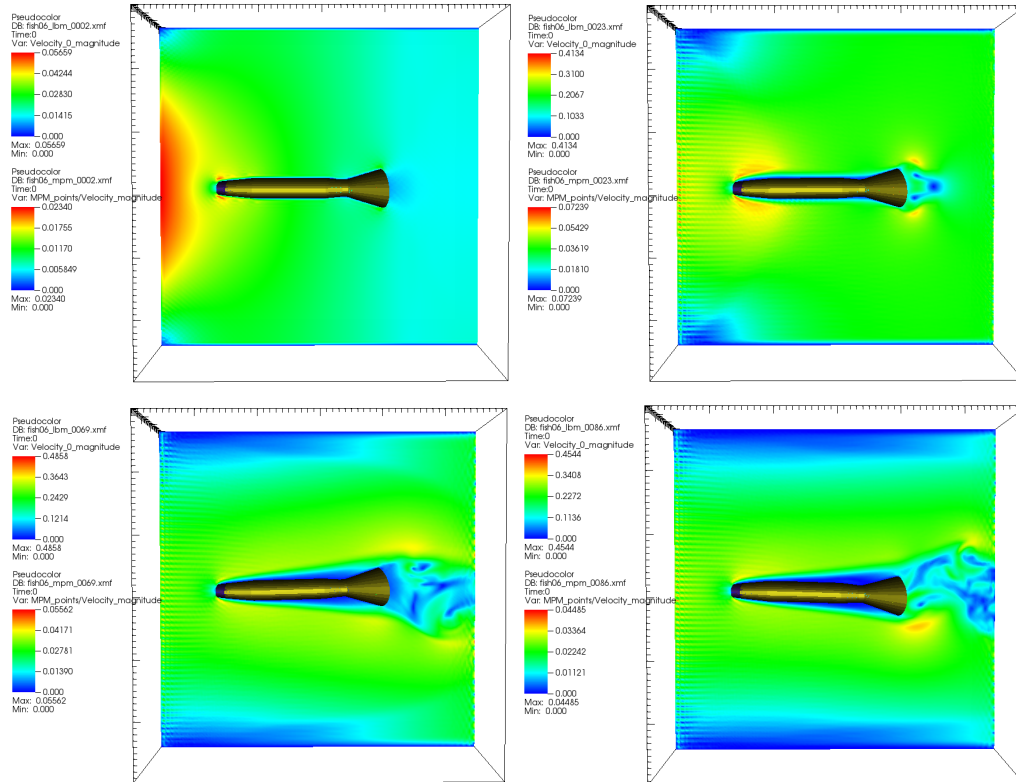


Figure 18: Snapshot of the fish motions and the fluid velocity field.